

Interfacial Photogating Effect for Hybrid Graphene-Based Photodetectors

Yifei Wang, Vinh X. Ho, Prashant Pradhan, Michael P. Cooney, and Nguyen Q. Vinh*

Cite This: *ACS Appl. Nano Mater.* 2021, 4, 8539–8545

Read Online

ACCESS |



Metrics & More



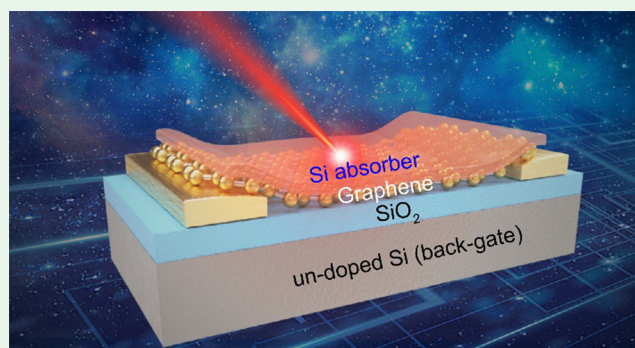
Article Recommendations



Supporting Information

ABSTRACT: Ultrafast and high-sensitive photodetectors operating from the deep-ultraviolet to near-infrared region at room temperature are essential for many applications such as analytical chemistry, optical positioning, biomedical imaging, and remote sensing. Toward high-performance photodetectors, hybrid colloid quantum dots/graphene photodetectors based on the photogating mechanism have been intensively studied. An ultrahigh sensitivity has been obtained in the range from 10^5 to 10^9 A/W but the major challenge of these configurations is the slow operating speed on the millisecond to second time scale. Manipulating the transferring of carriers at the interface of semiconductor nanostructures and graphene is an essential key to optimize the interfacial photogating effect. Here, we grow an absorber layer directly on graphene by e-beam evaporation to obtain a fast photoresponse time of the detectors. Thus, the gap between the high responsivity and fast response time can be bridged. The photodetectors indicate a high photoresponsivity of $\sim 2.5 \times 10^6$ A/W at low incident intensity on the order of femto-watts, a specific detectivity of $\sim 8.5 \times 10^{11}$ Jones, and a fast response process of ~ 20 ns together with a slow component of ~ 850 ns (response time of $< 1 \mu\text{s}$) under a drain-to-source bias of 100 mV. The study has provided a method to obtain high-performance photodetectors based on graphene with high responsivity and fast response time.

KEYWORDS: interfacial photogating, graphene, field-effect transistor, photodetection, hybrid silicon–graphene photodetectors



INTRODUCTION

Graphene has attracted strong interest for ultra-broadband photodetection from deep-ultraviolet to terahertz frequencies, in which various applications such as remote sensing, biomedical imaging, optical positioning, and optical communication require both fast speed and ultrahigh sensitivity.^{1–4} Ultrafast carrier mobility in single-layer graphene enables ultrafast speed operation.^{5,6} The intrinsic graphene-based photodetectors have shown photoresponse on the picosecond time scale.^{7–9} However, the poor absorption ($\sim 2.3\%$) and fast carrier recombination on the femtosecond time scale of the monolayer graphene limit the viability for weak-intensity light detection.^{10,11} The photoresponsivity is only about few milliamperes per watt.^{9,12}

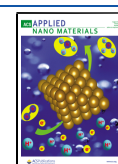
A number of proposed prototypes have been studied to improve the sensitivity for weak light detection of graphene. Graphene/silicon (Gr/Si) heterojunction devices have been realized for photodetection.^{13–16} In these devices, graphene contacts directly to silicon to form heterojunctions. On graphene field-effect transistor structures, interfacial photogating has been observed for the Gr/SiO₂/Si interface in the silicon substrate of devices.^{17–20} The photoresponsivity for this structure is typically about 1000 A/W. In another approach, the graphene photodetectors have been coupled with micro-

cavities, waveguides, optical antennas, and plasmonic structures to increase responsivity via the light-matter interaction in these structures.^{21–25} One of the promising approaches based on the photogating effect of hybrid of semiconductor nanostructures (i.e., colloidal quantum dots (CQDs), nanowires, and nanorods) and graphene can significantly enhance the responsivity and detectivity.^{26–30} In these hybrid nanoscale structures, electron and hole pairs are generated from light-absorbing nanostructures. One type of photogenerated carriers is trapped in the nanostructures, while the opposite type of charge transfers to graphene and quickly circulates in the graphene channel controlled by a source–drain voltage, leading to a photogating effect. Such photodetectors can obtain ultrahigh responsivity up to 10^9 A/W;^{26–29} however, the disadvantage of this approach is a slow response speed on the millisecond (even second) scales, preventing the high-speed photodetection.^{28,29,31} Obviously, we can only choose

Received: July 12, 2021

Accepted: July 28, 2021

Published: August 11, 2021



either ultrafast speed response or ultrasensitivity in the graphene-based photodetectors. In the nanostructure–graphene configurations, the nanostructures are typically synthesized by chemical methods with introducing catalysts and required ligand exchange before transferring on top of graphene, producing high trap density at the nanostructure/graphene interface or inside the nanostructures. To minimize the traps introduced from the catalysts or ligand exchange, we grow a thin absorber layer on top of graphene by electron-beam (e-beam) evaporation, avoiding contamination between graphene and the silicon absorber layer. The *in-situ* fabrication condition can guarantee the high quality of the absorber layer with less trap density and obtain an efficient process of charge transfer. A large contact area between the thin film and single-layer graphene provides an ultrafast process for carrier transferring from the thin film to graphene. These could increase the operating speed and still maintain the high gain for the photodetectors.

Here, we have demonstrated hybrid silicon–graphene (Si/Gr) photodetectors based on the photogating effect, in which a silicon absorber layer with a thickness of 10 nm was grown by the e-beam evaporation method. Our devices successfully balance the gap between the photoresponse speed and the high sensitivity. Specifically, the photodetectors show a high photoresponsivity of $\sim 2.5 \times 10^6$ A/W at low intensity on the order of femto-watts, a specific detectivity of $\sim 8.5 \times 10^{11}$ Jones, and an ultrafast rise time of ~ 20 ns under a drain-source bias of 100 mV. The study shows a method to obtain high-performance graphene photodetectors in the deep-ultraviolet (UV) to near-infrared (NIR) region.

FABRICATION AND CHARACTERIZATION

We have fabricated graphene field-effect transistors on the Si/SiO₂ substrate with an n-type silicon absorber layer on top of graphene. Initially, a 300 nm SiO₂ layer was thermally grown on an undoped silicon wafer. Photolithography, e-beam evaporation, and metal lift-off processes were used to form drain, source, and back-gate contacts (3 nm Cr and 100 nm Au). After that, a monolayer graphene was transferred to the Si/SiO₂ substrate.^{3,32,33} The monolayer graphene was confirmed by the Raman spectrum (Figure S2). A 10-nm n-type silicon absorber layer was grown on top of the graphene channel by the e-beam evaporation method with a growth rate of 0.1 Å/s. A schematic of the graphene field-effect transistors for photodetection is shown in Figure 1a, including source drain, back-gate contacts together with graphene, and the n-type silicon layer. Finally, the active size of the graphene channel was determined by photolithography and dry etching steps. The length or distance between source and drain, L , is 5 μm , and the width of the graphene channel, W , is 10 μm . The hybrid Si/Gr photodetector is illustrated in Figure S1. Atomic force microscopy (AFM) images of our graphene/silicon structure are shown in Figure S3. We made four sets of the devices at different times. Each set includes 15 devices. The results that we presented here are similar to other results from different devices. Our devices show repeatable results.

RESULTS AND DISCUSSION

The current–voltage (I – V) relationship with and without illumination of light at room temperature was measured by two Keithley units (Figure 1b). A Keithley 2450 was utilized to control the back-gate bias, V_{BG} , from -30 to 30 V. Another

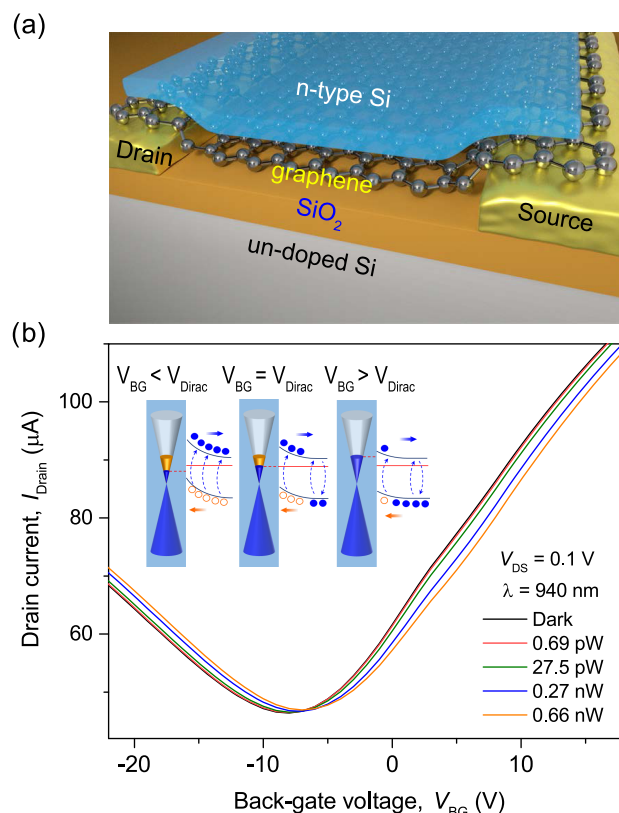


Figure 1. (a) Schematic of the graphene field-effect transistor devices for photodetection showing source drain, back-gate contacts together with graphene, and the n-type silicon layer. (b) Current–voltage characteristics of the hybrid Si/Gr photodetector with and without illumination ($\lambda = 940$ nm), $V_{\text{DS}} = 100$ mV at room temperature. The inset illustrates the schematic diagram of the energy band of the hybrid Si/Gr structure. The orange circles illustrate holes and blue dots present electrons.

Keithley 2450 was used to fix a drain-to-source bias, V_{DS} , of 100 mV and to collect the drain current, I_{D} . The I – V characteristic curves shift toward the positive of the back-gate voltage under illumination ($\lambda = 940$ nm). In other words, the charge neutrality point (CNP) voltage (V_{Dirac}) of the I – V characteristic curves moves toward the positive of the back-gate bias as the light intensity is varied from 10 fW to 0.66 nW. The drain current, I_{D} , increases with $V_{\text{BG}} < V_{\text{Dirac}}$ and decreases for $V_{\text{BG}} > V_{\text{Dirac}}$ (Figure 1b).

The detectors are sensitive to light, which can be described based on the interfacial photogating effect, as demonstrated in the energy band diagram (Figure 1b, inset). The work function of graphene is higher than that of the n-type silicon (i.e., absorber layer), so the height of the potential barrier between graphene and n-type silicon is in the range from 0.7 to 0.86 eV.³⁴ Thus, the energy bands of the n-type silicon are bent upward at the Si/Gr interface, forming a built-in potential between graphene and the silicon thin film.^{4,35} Electron–hole pairs are generated in the silicon absorber layer during the illumination and separated at the Si/Gr interface under the built-in electrical field. By applying the back-gate bias, the built-in electrical field can be manipulated quickly to speed up the injection of carriers into the graphene channel. Holes are transferred into the graphene channel. Under the varying of the back-gate voltage, the bending of bands at the Si/SiO₂ interface can be increased or decreased, resulting in an

increase or a decrease of the number of carriers injecting into graphene. In addition, the electron density of states in the n-type silicon absorber is much higher than that of graphene; thus, the Fermi level of graphene is very sensitive to its carrier concentration and the external electrical field.³⁶ The carrier concentration of the n-type silicon absorber layer ($\sim 10^{15} \text{ cm}^{-2}$) is also higher than that of graphene ($\sim 10^{12} \text{ cm}^{-2}$).³⁷ Therefore, the graphene's Fermi level is shifted more obviously than that of the silicon layer under the modulation of the back-gate bias. Under $V_{\text{BG}} \leq V_{\text{Dirac}}$ the potential barrier at the Si/Gr interface will be lifted up, which leads to the injection of holes into graphene. Because of the high carrier mobility in graphene, when holes were diffused into graphene, they move quickly to electrodes under the drain-source bias, V_{DS} . The thin absorber layer with a thickness of 10 nm acts as a quantum well, which confines electrons. As long as, a hole enters the electrode, a new one is introduced to the graphene channel to neutralize with the electron in the absorber layer. A combination of the fast transit time of holes in the graphene channel and the long confinement time of electrons in the silicon absorber layer results in a recirculation of holes between metal contacts. This gives rise to a high gain of the photocurrent for the hole-dominated channel. Under $V_{\text{BG}} > V_{\text{Dirac}}$ the potential barrier at the Si/Gr interface will be lower. There is a reduction in the number of holes transferring to the graphene channel from the silicon layer, resulting in a reduction of the dark current (a negative photocurrent) or an electron-dominated channel. The recirculation of holes in the graphene layer is a crucial factor of ultrahigh photoconductive gain in the hybrid Si/Gr structure detectors.

To shed light on the characteristics of the Si/Gr photo-detectors, we have performed the power dependence of photocurrent and calculated the photoresponsivity. The photocurrent is calculated by $I_{\text{ph}} = I_{\text{illumination}} - I_{\text{dark}}$ where $I_{\text{illumination}}$ and I_{dark} are the current under illumination and dark conditions, respectively. The photocurrent under different excitation power is presented as a function of the back-gate voltage and reaches a maximum value at $V_{\text{BG}} = 6 \text{ V}$ (Figure 2a). At this voltage, the bending of bands at the Si/Gr interface obtains a maximum efficiency for the photogating effect, thus, the highest photocurrent has been obtained. The photocurrent at $V_{\text{BG}} = 6 \text{ V}$ under different excitation power of the 940 nm laser is presented in Figure 2b. The photocurrent increases linearly under a weak illumination power from 7 fW to 1.5 pW and rises slowly under high radiation power. The detectors are extremely sensitive to light. With an illumination power $\sim 10 \text{ fW}$, a net photocurrent value of $\sim 10 \text{ nA}$ has been observed (Figure 2b, inset).

A large range of photodetection is an essential feature of photodetectors in many applications of imaging and remote sensing. The photoresponsivity of the devices has been determined, $R_{\text{ph}} = I_{\text{ph}}/P$. The photoresponsivity as a function of illumination power has been characterized (Figure 2b, inset). Under low excitation power, the linear power dependence of photocurrent has been detected in a large range of illumination power, resulting in a constant of the photoresponsivity. The detectors show a high photoresponsivity of $\sim 7.5 \times 10^5 \text{ A/W}$ at $\lambda = 940 \text{ nm}$ for almost three orders of magnitude of illumination power on the fW to pW scale, allowing for weak signal detection. Under the low illumination power regime, electrons and holes generated from the photoabsorption process are well separated, thus a higher number of photons will produce a higher electrical current.

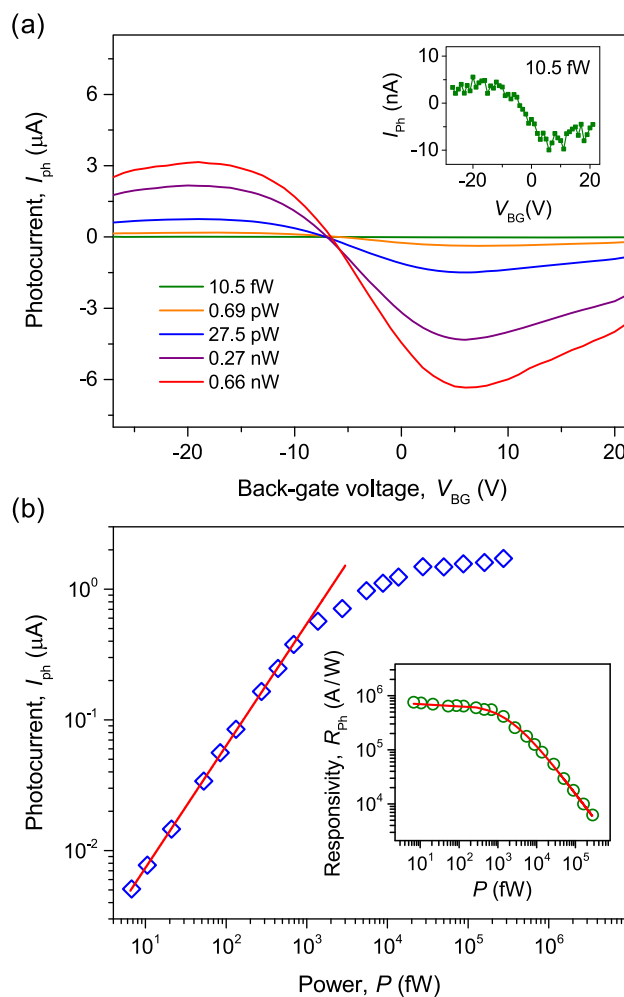


Figure 2. (a) Photocurrent as a function of back-gate voltage under different illumination power of a 940 nm light source. The inset shows the photocurrent under an illumination power of 10.5 fW. (b) Photocurrent as a function of illumination power at $V_{\text{BG}} = 6 \text{ V}$. The inset presents the photoresponsivity of the photodetector as a function of illumination power.

Under high power illumination, a higher number of electron–hole pairs are generated. Some holes recombine with electrons, and thus, these holes do not contribute to the photocurrent. Also, the number of photons also exceeds the absorption limitation of the thin-film silicon layer ($\sim 10 \text{ nm}$). Thus, the growth of the photocurrent with increasing power has been slow down, and the photoresponsivity is reduced at high illumination power. Note that we also observe the photo-response from the silicon substrate (Gr/SiO₂/Si), which is the same structure but without the n-type silicon absorber layer. The photoresponsivity of this structure shows a typical value of $\sim 1000 \text{ A/W}$,^{17–19} which is several orders of magnitude lower when compared with our results reported here.

The lifetime of carriers strongly depends on the carrier concentration or the illumination power. At a high illumination power, a high number carrier concentration has been introduced, they recombine, and thus, the average lifetime of the carriers will be shortened. The lifetime of carriers, T_{carrier} , as a function of the illumination power, P , can be expressed^{27,30}

$$T_{\text{carrier}} = \frac{T_0}{1 + (P/P_0)^{\gamma}} \quad (1)$$

where T_0 is the electron lifetime in the quantum well before it recombines with a hole under illumination power, P , γ is a fitting parameter, and P_0 is the illumination power at which the number of confined carriers reaches the saturation in the thin film. The number of carriers diffused into the graphene channel can be determined by

$$N_{\text{carrier}} = \alpha\eta N_{\text{ph}} T_{\text{carrier}} = \alpha\eta N_{\text{ph}} \frac{T_0}{1 + (P/P_0)^\gamma} \quad (2)$$

where α is the efficiency of carrier transferring from the silicon absorber layer into the graphene channel, η is the internal quantum efficiency of the carrier generation process in the silicon absorber layer, $N_{\text{ph}} = P/(h\nu)$ is the number of incident photons per unit time, and $h\nu$ is the photon energy. Thus, the relation between the photocurrent and the number of carriers can be expressed as

$$I_{\text{ph}} = q \frac{N_{\text{carrier}}}{T_{\text{trans}}} \quad (3)$$

where q is the elementary charge, $T_{\text{trans}} = \frac{L}{v_{\text{drift}}} = \frac{L}{\mu V_{\text{DS}} L^{-1}}$ is the transit time of carriers between drain and source contacts, L , and v_{drift} is the drift velocity. During the long confinement time of electrons in the silicon layer, holes recirculate between the metal contacts under the drain-source bias, V_{DS} , resulting in a high gain or responsivity of the hybrid Si/Gr photodetector. The photoresponsivity can be determined by the ratio of recirculated holes to incident photons per unit time^{28,30}

$$R_{\text{ph}} = \frac{I_{\text{ph}}}{P} = \frac{qN_{\text{carrier}}}{T_{\text{trans}}h\nu N_{\text{ph}}} = \alpha\eta \left(\frac{q}{h\nu} \right) \left(\frac{T_0}{T_{\text{trans}}} \right) \frac{1}{1 + (P/P_0)^\gamma} \quad (4)$$

The fast transit time of the carriers in graphene coupled with the long confinement time of the oppositely charged carriers in the silicon absorber layer gives rise to a high photoresponsivity, R_{ph} of $\sim 7.6 \times 10^5$ A/W, at $\lambda = 940$ nm, under the drain-to-source voltage, V_{DS} , of 100 mV. The reduction of the photoresponsivity at high illumination intensity indicates the depletion of photogenerated electron–hole pairs. The solid red line is the best fit to experimental data using eq 4 (Figure 2b, inset), from which $P_0 \sim 1.8$ pW and $\gamma \sim 0.85$ are obtained.

A fast response time of photodetectors is an important factor for the performance of the devices. To gain insight into the balance between the ultrafast response and ultrasensitivity of the Si/Gr photodetectors, we have characterized the operating speed of the photodetectors under $V_{\text{DS}} = 100$ mV at room temperature. We have used an acousto-optic modulator (AOM) to modulate a continuous-wave 940 nm laser into laser pulses with a rise time of 20 ns (or a bandwidth of 17.5 MHz). A Tektronix oscilloscope (a bandwidth of 5 GHz) is employed to record the photocurrent dynamics. Figure 3 shows the response of photocurrent with the laser pulse. The response and recovery times (or rise and fall times, respectively) defined as the time for photocurrent changing from 10 to 90% of the final value, are roughly ~ 1 and ~ 250 μs , respectively. The rise time consists of two components, including a fast, τ_{riseF} and a slow, τ_{riseS} , component. The rise time is fitted by an exponential function

$$I_{\text{ph}} = I_0 - A \exp\left(-\frac{t}{\tau_{\text{riseF}}}\right) - B \exp\left(-\frac{t}{\tau_{\text{riseS}}}\right) \quad (5)$$

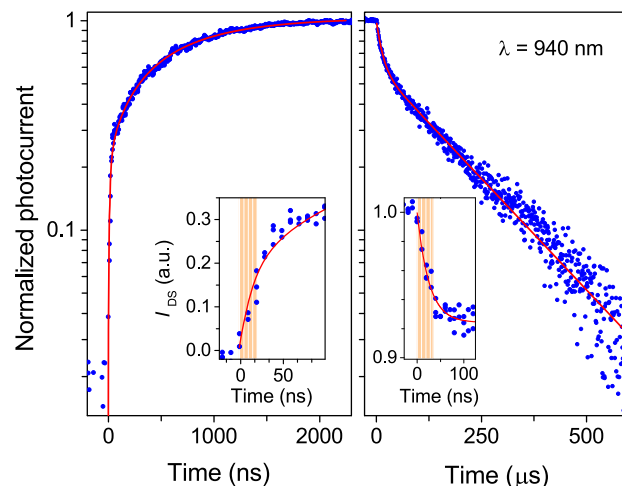


Figure 3. Time response of the hybrid Si/Gr photodetector under the excitation of the 940 nm laser pulses.

The fast rise time, $\tau_{\text{riseF}} \sim 20$ ns, has been observed, which is similar to the rise time of the laser pulses, while the slower time constant, $\tau_{\text{riseS}} \sim 850$ ns, represents the diffusion of charge carriers from the silicon absorber layer to graphene. The carrier mobility, μ , was estimated about ~ 6450 $\text{cm}^2 \text{V}^{-1} \text{s}^{-1}$ (Figure S4), and thus, the average transit time of carriers between the source and drain contacts is about 0.2 ns. The rise time observed here is limited by the rise time of the laser pulses ~ 20 ns. The recovery time data of the photodetector can be analyzed with the decay exponential function

$$I_{\text{ph}} = C \exp\left(-\frac{t}{\tau_{\text{fallF}}}\right) + D \exp\left(-\frac{t}{\tau_{\text{fallS}}}\right) \quad (6)$$

The fast recovery time constant, $\tau_{\text{fallF}} \sim 200$ ns, is the recombination time of holes at the Si/Gr interfacial with confined electrons in the thin film. The slower time constant, $\tau_{\text{fallS}} \sim 250$ μs , is contributed by the diffusion time of holes from graphene back to the absorber layer for the recombination with electrons when the illumination is turned off. The observation of the response and recovery times is similar in the whole wavelength range studied here. The rise time in the NIR region of these devices is faster than those of previous reports, which is about few orders of magnitude.^{27–29,31,38,39} In addition, the photoresponse of these detectors is remarkably stable without drift of photocurrent for a long illumination time over 40 000 on/off cycles (Figure S6). The performance remains stable for many months in ambient conditions.

Although the hybrid CQDs/graphene photodetectors have provided very high responsivity ($\sim 10^5$ to 10^9 A/W), typically, the response time is on the time scale of a millisecond or even seconds.^{28,29,31,38} The CQDs transferred on top of graphene are typically synthesized by wet-chemical and/or physical methods, including catalysts, and the ligand exchanges,⁴⁰ containing a high trap density at CQDs/graphene interfaces or in the CQDs. These traps have a long lifetime on the second time scale, thus, the devices obtained a high gain. However, these devices will possess a long response and recovery times.²⁸ Instead of using CQDs, we grow the absorber layer on top of graphene by the e-beam evaporation method. The *in-situ* fabrication condition can substantially reduce the density of surface traps (e.g., dangling bonds and defects at the Si/Gr interface), providing a high quality of the absorber layer and

obtaining an efficient process for charge transfer. Therefore, a fast-operating speed has been obtained, and a high gain has been maintained. The rise time values are faster than previous studies about few orders of magnitude, and the photoresponsivity is in the range of 10^6 A/W. Using the configuration, we can balance between high-speed response and ultrasensitivity.

The hybrid Si/Gr photodetectors have demonstrated a large detection range from the deep-UV to NIR region at room temperature with a high gain (Figure 4). The 940 nm diode

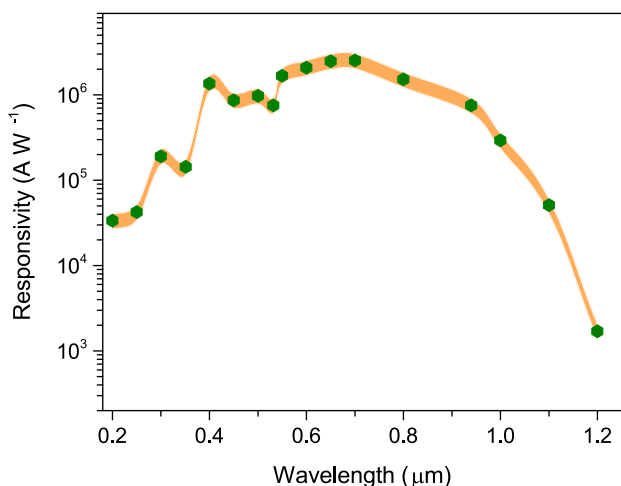


Figure 4. Photoresponsivity of the hybrid Si/Gr photodetector as a function of photon wavelength in the deep-UV to NIR region.

laser and an Edmund Deuterium/Tungsten lamp with a wavelength from 190 nm to $2.6 \mu\text{m}$ have been employed to characterize the performance of the photodetectors. Using narrow band-pass filters, we have extracted light with a narrow bandwidth from the Deuterium/Tungsten lamp. The photoresponsivity of these detectors is on the order of 10^3 to 10^6 A/W from the deep-UV (200 nm) to the NIR (1200 nm) region. Specifically, the photoresponsivity at 700 nm is 2.5×10^6 A/W. The photocurrent and photoresponsivity at several wavelengths are presented in the Supporting Information (Figure S8). The photoresponsivity of our detectors is comparable with two-dimensional (2D) material-based photodetectors such as graphene nanoribbons,⁴¹ graphene quantum dots,⁴² black arsenic phosphorus⁴³ and black phosphorus,^{44,45} and PtSe₂,⁴⁶ however, the response time is a few orders of magnitude faster.

To evaluate the performance of photodetectors, the sensitivity is specified by the noise equivalent power (NEP) and the specific detectivity (D^*). NEP is the output signal of an incident light equal to the detector noise level (i.e., the root mean square noise level of the dark current) divided by the responsivity of the detector within a standard bandwidth of 1 Hz, given by^{32,47,48}

$$\text{NEP} = \frac{\sqrt{S_1(1/f) + S_1(\text{thermal}) + S_1(\text{shot})}}{R_{\text{ph}}} \quad (7)$$

where $S_1(1/f)$, $S_1(\text{thermal})$, and $S_1(\text{shot})$ are the power spectral density of the $1/f$, thermal, and shot noise, respectively, for 1 Hz bandwidth. The power spectral density of the $1/f$ noise of the Si/Gr photodetector is presented in Figure 5 (inset). The power spectral density values of $S_1(1/f)$, $S_1(\text{thermal})$, and

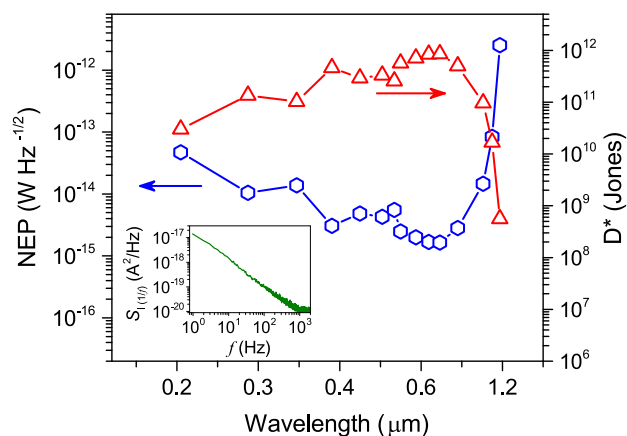


Figure 5. Noise equivalent power (NEP) and specific detectivity (D^*) of the hybrid Si/Gr photodetector as a function photon wavelength. The inset shows the power spectral density of the $1/f$ noise of the Si/Gr photodetector under $V_{\text{DS}} = 100$ mV.

$S_1(\text{shot})$ noise for the 1 Hz bandwidth are 8.8×10^{-15} , 6.61×10^{-25} , and 1.25×10^{-23} A²/Hz at $V_{\text{DS}} = 100$ mV. The measurement and estimation are presented in the Supporting Information. Under $V_{\text{DS}} = 100$ mV, we have obtained the NEP values from 2.5×10^{-12} (at $\lambda = 1200$ nm) to 1.6×10^{-15} W Hz^{-1/2} (at $\lambda = 700$ nm) in the detection range from the deep-UV to NIR region. From the NEP values, we have calculated the specific detectivity, D^* , as presented in Figure 5.

$$D^* = \frac{\sqrt{A}}{\text{NEP}} \quad (8)$$

where A is the area of the graphene channel. The specific detectivity, D^* , is in the range from 5.6×10^8 to 8.5×10^{11} Jones (cm Hz^{1/2}/W) in the deep-UV to NIR region. The significantly small NEP values indicate that the hybrid Si/Gr photodetectors are suitable for weak light detection and switching/photometry.

CONCLUSIONS

In conclusion, we have fabricated and demonstrated the hybrid Si/Gr photodetectors based on the interfacial photogating effect with high responsivity and fast response speed. The thin-film absorber layer of photodetectors has been grown by e-beam evaporation. These devices allow us to detect a weak illumination power on the femto-watt scale and with a fast response time. The photodetectors are highly sensitive in a large range of wavelengths from the deep-UV to NIR region with a responsivity of $\sim 10^6$ A/W.

ASSOCIATED CONTENT

Supporting Information

The Supporting Information is available free of charge at <https://pubs.acs.org/doi/10.1021/acsnm.1c01931>.

Details for graphene field-effect transistor fabrication, electrical setup, I - V transfer characteristics, noise characterization (PDF)

AUTHOR INFORMATION

Corresponding Author

Nguyen Q. Vinh – Department of Physics and Center for Soft Matter and Biological Physics, Virginia Tech, Blacksburg,

Virginia 24061, United States; orcid.org/0000-0002-3071-1722; Phone: 1-540-231-3158; Email: vinh@vt.edu

Authors

Yifei Wang – Department of Physics and Center for Soft Matter and Biological Physics, Virginia Tech, Blacksburg, Virginia 24061, United States

Vinh X. Ho – Department of Physics and Center for Soft Matter and Biological Physics, Virginia Tech, Blacksburg, Virginia 24061, United States; orcid.org/0000-0001-5413-9030

Prashant Pradhan – Department of Physics and Center for Soft Matter and Biological Physics, Virginia Tech, Blacksburg, Virginia 24061, United States

Michael P. Cooney – NASA Langley Research Center, Hampton, Virginia 23681, United States

Complete contact information is available at:
<https://pubs.acs.org/10.1021/acsnm.1c01931>

Notes

The authors declare no competing financial interest.

ACKNOWLEDGMENTS

The authors gratefully acknowledge the financial support of this effort by the Earth Science Technology Office (ESTO), NASA.

REFERENCES

- (1) Koppens, F. H. L.; Mueller, T.; Avouris, P.; Ferrari, A. C.; Vitiello, M. S.; Polini, M. Photodetectors based on graphene, other two-dimensional materials and hybrid systems. *Nat. Nanotechnol.* **2014**, *9*, 780–793.
- (2) Bonaccorso, F.; Sun, Z.; Hasan, T.; Ferrari, A. C. Graphene photonics and optoelectronics. *Nat. Photonics* **2010**, *4*, 611–622.
- (3) Novoselov, K. S.; Jiang, D.; Schedin, F.; Booth, T. J.; Khotkevich, V. V.; Morozov, S. V.; Geim, A. K. Two-dimensional atomic crystals. *Proc. Natl. Acad. Sci. U.S.A.* **2005**, *102*, 10451–10453.
- (4) Das, S.; Pandey, D.; Thomas, J.; Roy, T. The Role of Graphene and Other 2D Materials in Solar Photovoltaics. *Adv. Mater.* **2019**, *31*, No. 1802722.
- (5) Dean, C. R.; Young, A. F.; Meric, I.; Lee, C.; Wang, L.; Sorgenfrei, S.; Watanabe, K.; Taniguchi, T.; Kim, P.; Shepard, K. L.; Hone, J. Boron nitride substrates for high-quality graphene electronics. *Nat. Nanotechnol.* **2010**, *5*, 722–726.
- (6) Yu, J.; Liu, G. X.; Sumant, A. V.; Goyal, V.; Balandin, A. A. Graphene-on-Diamond Devices with Increased Current-Carrying Capacity: Carbon sp²-on-sp³ Technology. *Nano Lett.* **2012**, *12*, 1603–1608.
- (7) Urich, A.; Unterrainer, K.; Mueller, T. Intrinsic Response Time of Graphene Photodetectors. *Nano Lett.* **2011**, *11*, 2804–2808.
- (8) Winnerl, S.; Orlita, M.; Plochocka, P.; Kossacki, P.; Potemski, M.; Winzer, T.; Malic, E.; Knorr, A.; Sprinkle, M.; Berger, C.; de Heer, W. A.; Schneider, H.; Helm, M. Carrier Relaxation in Epitaxial Graphene Photoexcited Near the Dirac Point. *Phys. Rev. Lett.* **2011**, *107*, No. 237401.
- (9) Xia, F. N.; Mueller, T.; Lin, Y. M.; Valdes-Garcia, A.; Avouris, P. Ultrafast graphene photodetector. *Nat. Nanotechnol.* **2009**, *4*, 839–843.
- (10) Nair, R. R.; Blake, P.; Grigorenko, A. N.; Novoselov, K. S.; Booth, T. J.; Stauber, T.; Peres, N. M. R.; Geim, A. K. Fine structure constant defines visual transparency of graphene. *Science* **2008**, *320*, 1308.
- (11) Low, T.; Avouris, P. Graphene Plasmonics for Terahertz to Mid-Infrared Applications. *ACS Nano* **2014**, *8*, 1086–1101.
- (12) Park, J.; Ahn, Y. H.; Ruiz-Vargas, C. Imaging of Photocurrent Generation and Collection in Single-Layer Graphene. *Nano Lett.* **2009**, *9*, 1742–1746.
- (13) Chen, Z. F.; Cheng, Z. Z.; Wang, J. Q.; Wan, X.; Shu, C.; Tsang, H. K.; Ho, H. P.; Xu, J. B. High Responsivity, Broadband, and Fast Graphene/Silicon Photodetector in Photoconductor Mode. *Adv. Opt. Mater.* **2015**, *3*, 1207–1214.
- (14) Liu, F. Z.; Kar, S. Quantum Carrier Reinvestment-Induced Ultrahigh and Broadband Photocurrent Responses in Graphene - Silicon junctions. *ACS Nano* **2014**, *8*, 10270–10279.
- (15) Li, X. M.; Zhu, M.; Du, M. D.; Lv, Z.; Zhang, L.; Li, Y. C.; Yang, Y.; Yang, T. T.; Li, X.; Wang, K. L.; Zhu, H. W.; Fang, Y. High Detectivity Graphene-Silicon Heterojunction Photodetector. *Small* **2016**, *12*, 595–601.
- (16) Scagliotti, M.; Salvato, M.; De Crescenzi, M.; Mishra, N.; Fabbri, F.; Misekic, V.; Coletti, C.; Catone, D.; Di Mario, L.; Boscardin, M.; Castrucci, P. Large-area, high-responsivity, fast and broadband graphene/n-Si photodetector. *Nanotechnology* **2021**, *32*, No. 155504.
- (17) Shimatani, M.; Ogawa, S.; Fujisawa, D.; Okuda, S.; Kanai, Y.; Ono, T.; Matsumoto, K. Giant Dirac point shift of graphene phototransistors by doped silicon substrate current. *AIP Adv.* **2016**, *6*, No. 035113.
- (18) Guo, X. T.; Wang, W. H.; Nan, H. Y.; Yu, Y. F.; Jiang, J.; Zhao, W. W.; Li, J. H.; Zafar, Z.; Xiang, N.; Ni, Z. H.; Hu, W. D.; You, Y. M.; Ni, Z. H. High-performance graphene photodetector using interfacial gating. *Optica* **2016**, *3*, 1066–1070.
- (19) Luo, F.; Zhu, M. J.; Tan, Y.; Sun, H. H.; Luo, W.; Peng, G.; Zhu, Z. H.; Zhang, X. A.; Qin, S. Q. High responsivity graphene photodetectors from visible to near-infrared by photogating effect. *AIP Adv.* **2018**, *8*, No. 115106.
- (20) Ogawa, S.; Shimatani, M.; Fukushima, S.; Okuda, S.; Kanai, Y.; Ono, T.; Matsumoto, K. Broadband photoresponse of graphene photodetector from visible to long-wavelength infrared wavelengths. *Opt. Eng.* **2019**, *58*, No. 057106.
- (21) Echtermeyer, T. J.; Britnell, L.; János, P. K.; Lombardo, A.; Gorbachev, R. V.; Grigorenko, A. N.; Geim, A. K.; Ferrari, A. C.; Novoselov, K. S. Strong plasmonic enhancement of photovoltage in graphene. *Nat. Commun.* **2011**, *2*, No. 458.
- (22) Fang, Z. Y.; Liu, Z.; Wang, Y. M.; Ajayan, P. M.; Nordlander, P.; Halas, N. J. Graphene-Antenna Sandwich Photodetector. *Nano Lett.* **2012**, *12*, 3808–3813.
- (23) Furchi, M.; Urich, A.; Pospischil, A.; Lilley, G.; Unterrainer, K.; Detz, H.; Klang, P.; Andrews, A. M.; Schrenk, W.; Strasser, G.; Mueller, T. Microcavity-Integrated Graphene Photodetector. *Nano Lett.* **2012**, *12*, 2773–2777.
- (24) Yao, Y.; Shankar, R.; Rauter, P.; Song, Y.; Kong, J.; Loncar, M.; Capasso, F. High-Responsivity Mid-Infrared Graphene Detectors with Antenna-Enhanced Photocurrent Generation and Collection. *Nano Lett.* **2014**, *14*, 3749–3754.
- (25) Jiang, H.; Nie, C. B.; Fu, J. T.; Tang, L. L.; Shen, J.; Sun, F. Y.; Sun, J. X.; Zhu, M.; Feng, S. L.; Liu, Y.; Shi, H. F.; Wei, X. Z. Ultrasensitive and fast photoresponse in graphene/silicon-on-insulator hybrid structure by manipulating the photogating effect. *Nanophotonics* **2020**, *9*, 3663–3672.
- (26) Dang, V. Q.; Trung, T. Q.; Duy, L. T.; Kim, B. Y.; Siddiqui, S.; Lee, W.; Lee, N. E. High-Performance Flexible Ultraviolet (UV) Phototransistor Using Hybrid Channel of Vertical ZnO Nanorods and Graphene. *ACS Appl. Mater. Interfaces* **2015**, *7*, 11032–11040.
- (27) Guo, W. H.; Xu, S. G.; Wu, Z. F.; Wang, N.; Loy, M. M. T.; Du, S. W. Oxygen-Assisted Charge Transfer Between ZnO Quantum Dots and Graphene. *Small* **2013**, *9*, 3031–3036.
- (28) Konstantatos, G.; Badioli, M.; Gaudreau, L.; Osmond, J.; Bernechea, M.; de Arquer, F. P. G.; Gatti, F.; Koppens, F. H. L. Hybrid graphene-quantum dot phototransistors with ultrahigh gain. *Nat. Nanotechnol.* **2012**, *7*, 363–368.
- (29) Ni, Z. Y.; Ma, L. L.; Du, S. C.; Xu, Y.; Yuan, M.; Fang, H. H.; Wang, Z.; Xu, M. S.; Li, D. S.; Yang, J. Y.; Hu, W. D.; Pi, X. D.; Yang, D. R. Plasmonic Silicon Quantum Dots Enabled High-Sensitivity

Ultrabroadband Photodetection of Graphene-Based Hybrid Phototransistors. *ACS Nano* **2017**, *11*, 9854–9862.

(30) Shao, D. L.; Gao, J.; Chow, P.; Sun, H. T.; Xin, G. Q.; Sharma, P.; Lian, J.; Koratkar, N. A.; Sawyer, S. Organic-Inorganic Heterointerfaces for Ultrasensitive Detection of Ultraviolet Light. *Nano Lett.* **2015**, *15*, 3787–3792.

(31) Sun, Z. H.; Liu, Z. K.; Li, J. H.; Tai, G. A.; Lau, S. P.; Yan, F. Infrared Photodetectors Based on CVD-Grown Graphene and PbS Quantum Dots with Ultrahigh Responsivity. *Adv. Mater.* **2012**, *24*, 5878–5883.

(32) Wang, Y.; Ho, V. X.; Henschel, Z. N.; Cooney, M. P.; Vinh, N. Q. Effect of High-K Dielectric Layer on 1/f Noise Behavior in Graphene Field-Effect Transistors. *ACS Appl. Nano Mater.* **2021**, *4*, 3647–3653.

(33) Ho, V. X.; Wang, Y. F.; Cooney, M. P.; Vinh, N. Q. Graphene-Ta₂O₅ heterostructure enabled high performance, deep-ultraviolet to mid-infrared photodetection. *Nanoscale* **2021**, *13*, 10526–10535.

(34) Di Bartolomeo, A. Graphene Schottky diodes: An experimental review of the rectifying graphene/semiconductor heterojunction. *Phys. Rep.* **2016**, *606*, 1–58.

(35) Novikov, A. Experimental measurement of work function in doped silicon surfaces. *Solid-State Electron.* **2010**, *54*, 8–13.

(36) Chen, C. C.; Chang, C. C.; Li, Z.; Levi, A. F. J.; Cronin, S. B. Gate tunable graphene-silicon Ohmic/Schottky contacts. *Appl. Phys. Lett.* **2012**, *101*, No. 223113.

(37) Kim, M. S.; Kim, M.; Son, S.; Cho, S. Y.; Lee, S.; Won, D. K.; Ryu, J.; Bae, I.; Kim, H. M.; Kim, K. B. Sheet Resistance Analysis of Interface-Engineered Multilayer Graphene: Mobility Versus Sheet Carrier Concentration. *ACS Appl. Mater. Interfaces* **2020**, *12*, 30932–30940.

(38) Liu, C. H.; Chang, Y. C.; Norris, T. B.; Zhong, Z. H. Graphene photodetectors with ultra-broadband and high responsivity at room temperature. *Nat. Nanotechnol.* **2014**, *9*, 273–278.

(39) Chen, S. Y.; Lu, Y. Y.; Shih, F. Y.; Ho, P. H.; Chen, Y. F.; Chen, C. W.; Chen, Y. T.; Wang, W. H. Biologically inspired graphene-chlorophyll phototransistors with high gain. *Carbon* **2013**, *63*, 23–29.

(40) Dong, A. G.; Ye, X. C.; Chen, J.; Kang, Y. J.; Gordon, T.; Kikkawa, J. M.; Murray, C. B. A Generalized Ligand-Exchange Strategy Enabling Sequential Surface Functionalization of Colloidal Nanocrystals. *J. Am. Chem. Soc.* **2011**, *133*, 998–1006.

(41) Yu, X. C.; Dong, Z. G.; Liu, Y. P.; Liu, T.; Tao, J.; Zeng, Y. Q.; Yang, J. K. W.; Wang, Q. J. A high performance, visible to mid-infrared photodetector based on graphene nanoribbons passivated with HfO₂. *Nanoscale* **2016**, *8*, 327–332.

(42) Zhang, Y.; Liu, T.; Meng, B.; Li, X. H.; Liang, G. Z.; Hu, X. N.; Wang, Q. J. Broadband high photoresponse from pure monolayer graphene photodetector. *Nat. Commun.* **2013**, *4*, No. 1811.

(43) Long, M. S.; Gao, A. Y.; Wang, P.; Xia, H.; Ott, C.; Pan, C.; Fu, Y. J.; Liu, E. F.; Chen, X. S.; Lu, W.; Nilges, T.; Xu, J. B.; Wang, X. M.; Hu, W. D.; Miao, F. Room temperature high-detectivity mid-infrared photodetectors based on black arsenic phosphorus. *Sci. Adv.* **2017**, *3*, No. e1700589.

(44) Chen, X. L.; Lu, X. B.; Deng, B. C.; Sinai, O.; Shao, Y. C.; Li, C.; Yuan, S. F.; Tran, V.; Watanabe, K.; Taniguchi, T.; Naveh, D.; Yang, L.; Xia, F. N. Widely tunable black phosphorus mid-infrared photodetector. *Nat. Commun.* **2017**, *8*, No. 1672.

(45) Amani, M.; Regan, E.; Bullock, J.; Ahn, G. H.; Javey, A. Mid-Wave Infrared Photoconductors Based on Black Phosphorus-Arsenic Alloys. *ACS Nano* **2017**, *11*, 11724–11731.

(46) Yu, X. C.; Yu, P.; Wu, D.; Singh, B.; Zeng, Q. S.; Lin, H.; Zhou, W.; Lin, J. H.; Suenaga, K.; Liu, Z.; Wang, Q. J. Atomically thin noble metal dichalcogenide: a broadband mid-infrared semiconductor. *Nat. Commun.* **2018**, *9*, No. 1545.

(47) Kufer, D.; Konstantatos, G. Photo-FETs: Phototransistors Enabled by 2D and OD Nanomaterials. *ACS Photonics* **2016**, *3*, 2197–2210.

(48) Kayyalha, M.; Chen, Y. P. Observation of reduced 1/f noise in graphene field effect transistors on boron nitride substrates. *Appl. Phys. Lett.* **2015**, *107*, No. 113101.

SUPPORTING INFORMATION

Interfacial Photogating Effect for Hybrid Graphene-Based Photodetectors

Yifei Wang,¹ Vinh X. Ho,¹ Prashant Pradhan,¹ Michael P. Cooney,² and Nguyen Q. Vinh^{1*}

¹ Department of Physics and Center for Soft Matter and Biological Physics, Virginia Tech, Blacksburg, VA 24061, USA

² NASA Langley Research Center, Hampton, Virginia 23681, USA

* Corresponding author: vinh@vt.edu; phone: 1-540-231-3158

1. Device fabrication

The graphene field-effect transistors (Gr-FETs) for photodetection have been fabricated on an un-doped silicon (Si) wafer. A 300-nm silicon dioxide (SiO₂) was grown thermally on the Si substrate at 1050 °C. Metal contacts including source, drain, and back-gate (3-nm Cr and 100-nm Au metal films) on the Si/SiO₂ substrate were formed by using photolithography, electron beam thermal evaporation, lift-off, etching processes. After the lift-off process, the Si/SiO₂ wafer with metal contacts was cleaned in oxygen plasma for 4 minutes to eliminate photoresist residue.

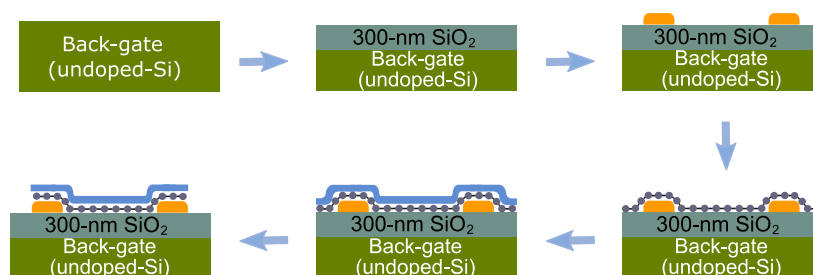


Figure S1. Schematic diagram showing fabrication steps of hybrid Si/Gr photodetectors.

A single-layer graphene grown by chemical vapor deposition (CVD) on a copper foil from Graphenea Inc. was transferred onto the Si/SiO₂ substrate with metal contacts.¹⁻⁵ The CVD graphene on the copper foil was spin-coated by poly-(methyl-methacrylate) (PMMA), after that a 0.3 M ammonium persulfate solution was used to remove the copper. Graphene with the PMMA film was rinsed with deionized water for 10

minutes and transferred onto the Si/SiO₂ substrate with electrodes. The structure was baked at 85 °C for 10 minutes, then at 135 °C for 20 minutes. The PMMA is removed by acetone for 1 hour, followed by IPA for 30 minutes. Photolithography and oxygen plasma etching were employed to fabricate a (5 × 10) μm² graphene pattern.³⁻⁴ A schematic diagram of the hybrid silicon/graphene (Si/Gr) photodetectors is illustrated in Figure S1.

2. Raman spectrum

A Raman spectrum was measured by using a WITec UHTS 300 micro-Raman spectrometer under the excitation of a 663.1-nm laser to evaluate the quality of graphene before growing a n-type Si absorber layer. Figure S2 reveals the high quality of a monolayer graphene with two peaks at ~ 2690 cm⁻¹ (2D band) and ~ 1585 cm⁻¹ (G band). The 2D band has only a single component with a FWHM of 33 cm⁻¹. The intensity ratio of the 2D peak to the G peak, I_{2D}/I_G , is 6.8, which confirms the high quality of the monolayer graphene.⁶ In addition, the D band of ~ 1350 cm⁻¹ presenting graphene defects from the graphene transferring process was not observed.⁷ Thus, the transferring graphene process can obtain the high-quality of the monolayer graphene.

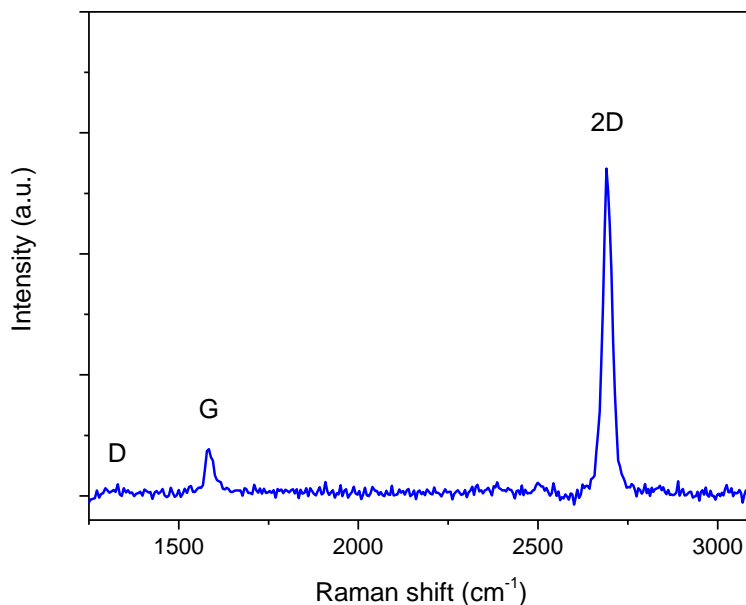


Figure S2. The Raman spectrum of a CVD monolayer graphene on Si/SiO₂.

2. Atomic force microscope images

To verify the morphology of the n-type Si absorber thin film, atomic force microscope (AFM) experiments have been performed. Figure S3 shows an AFM image of the n-type Si absorber thin film with a size of 1 × 1 μm² on graphene. The film has a roughness of less than 3 nm.

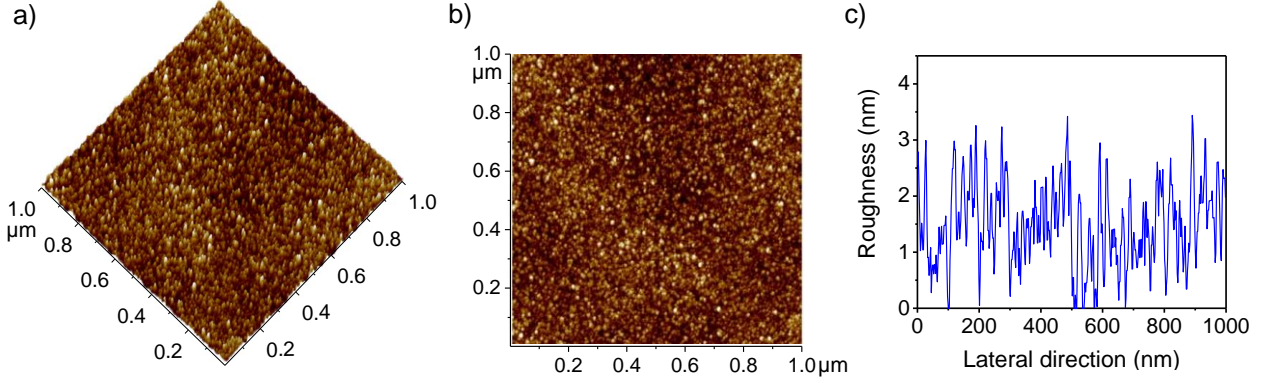


Figure S3. AFM images of the n-type silicon absorber thin film on graphene devices (a) three-dimensional view, and (b) top-view, and (c) roughness of the surface.

3. Carrier mobility in graphene devices

The carrier mobility in graphene devices can be extracted by fitting the resistance – voltage (R-V) characteristic curve (Figure S3) to the expression.⁸⁻¹⁰

$$R = 2R_c + R_{ch} = 2R_c + \frac{L/W}{nq\mu} \quad (S1)$$

$$n = \sqrt{n_0^2 + n_g^2} = \sqrt{n_0^2 + \left(\frac{C_G}{q}(V_{BG} - V_D)\right)^2} \quad (S2)$$

where R_c is the contact resistance, R_{ch} is the graphene channel resistance, L is the length or distance between source and drain, W is the width of the graphene channel, n_g is the density of charged carriers generated by a voltage on the back-gate, V_{BG} , away from the charge neutrality point voltage, V_D , (the Dirac point), n_0 is the carrier density resulting from charged impurities at the interface, q is the elementary charge, and $C_G = \frac{\epsilon\epsilon_0}{d}$ is the gate capacitance per unit area with the thickness of the SiO₂ layer, d , of 300 nm, the vacuum permittivity, ϵ_0 , and the SiO₂ dielectric constant, ϵ , of ~ 3.9 .¹¹ The capacitance of the 300-nm SiO₂ dielectric layer is ~ 11.5 nF/cm². The red curve in Figure S3 presents the best fit to the R-V characteristic data using Eqs 1 and 2. We have obtained the carrier mobility in the graphene devices of ~ 6450 cm²/(V·s).

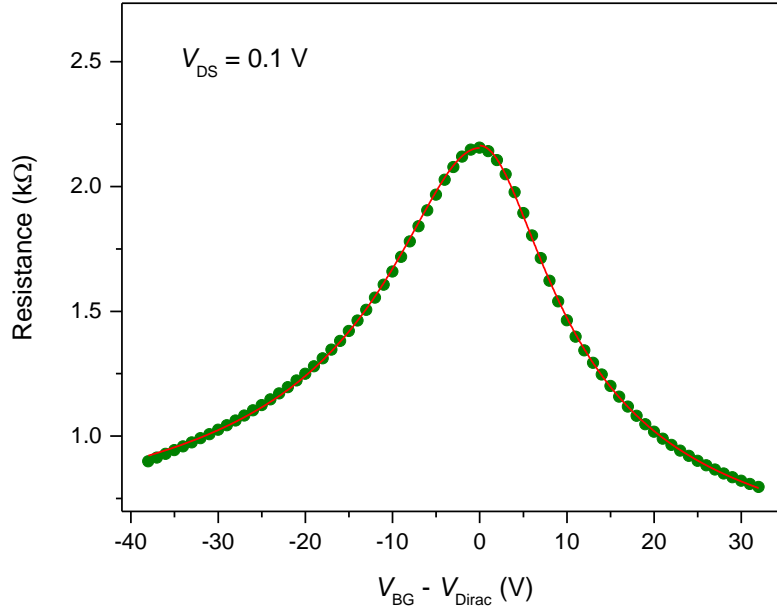


Figure S4. Resistance – voltage transfer characteristics of a hybrid Si/Gr photodetector ($L = 5 \mu\text{m}$, and $W = 10 \mu\text{m}$) under $V_{\text{DS}} = 100 \text{ mV}$.

4. Time-dependent photovoltage response

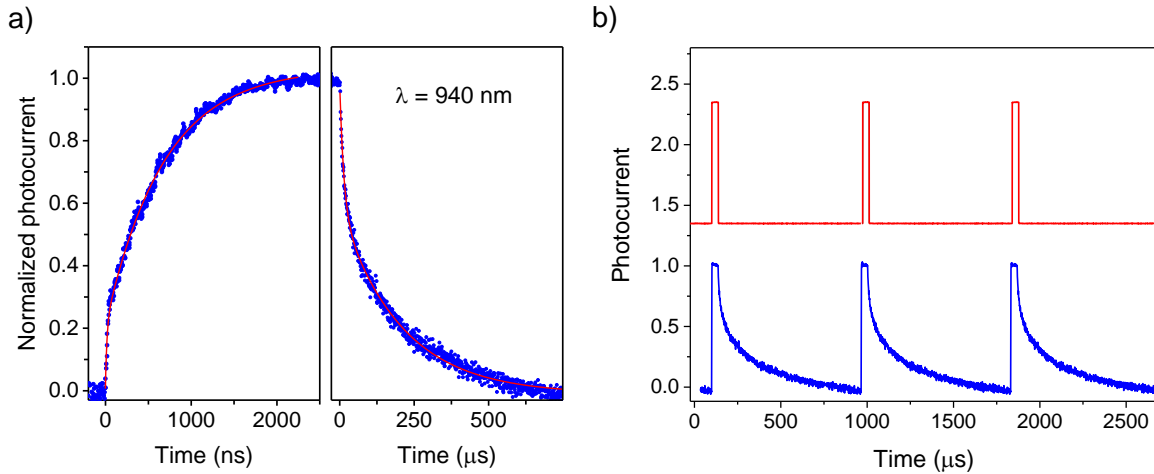


Figure S5. (a) The time response of the hybrid Si/Gr photodetector under the excitation of the 940-nm laser pulses in the linear scale. (b) The transient photo-response of the device reacts with illumination light.

The photocurrent response to a periodic on/off illumination was collected as a function of time to evaluate the long-term repeatable behavior. Figure S4 shows a result of reproducible tests. The detector was measured under $\sim 40,000$ on/off cycles. The fluctuation of photocurrent in the entire dataset is less than $\pm 5\%$ (main figure) and the current fluctuated less than $\pm 1\%$ for any 20 on/off cycles (inset), with no detection of fluctuation in current. The devices remain stable for many months in ambient conditions.

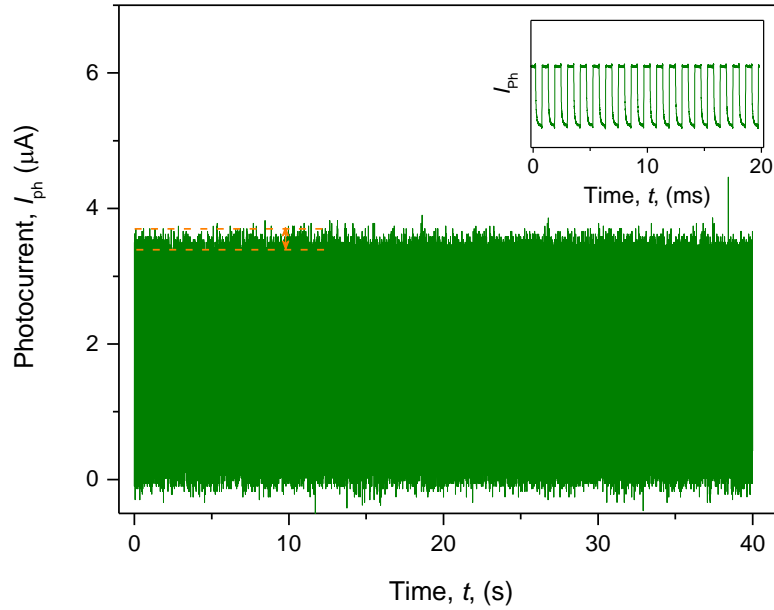


Figure S6. The photocurrent response under an on/off illumination

5. Power and voltage dependence measurements

The photo-responsivity, R_{ph} , and photocurrent, I_{ph} , as a function of back-gate voltage (Figure S7) and illumination power with different illumination wavelengths from the deep-UV to NIR region (Figure S8) have been characterized.

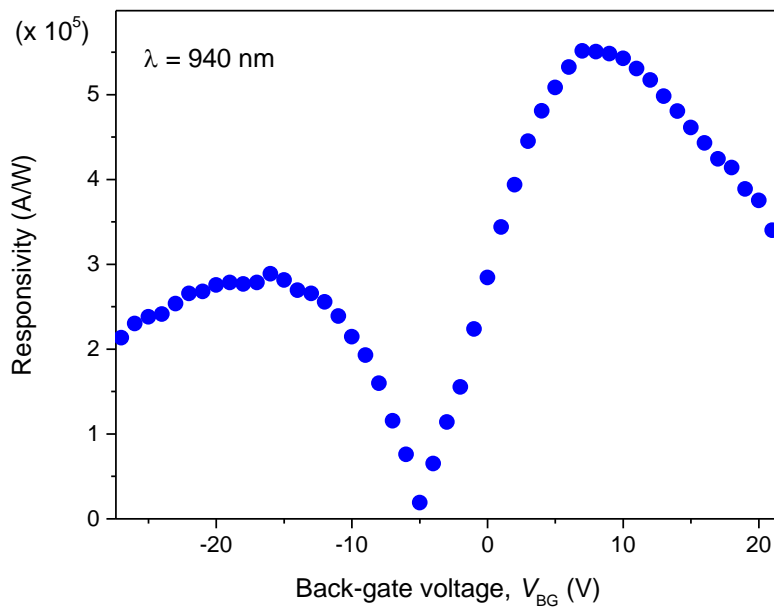


Figure S7. Photo-responsivity as a function of back-gate voltage at $\lambda = 940$ nm.

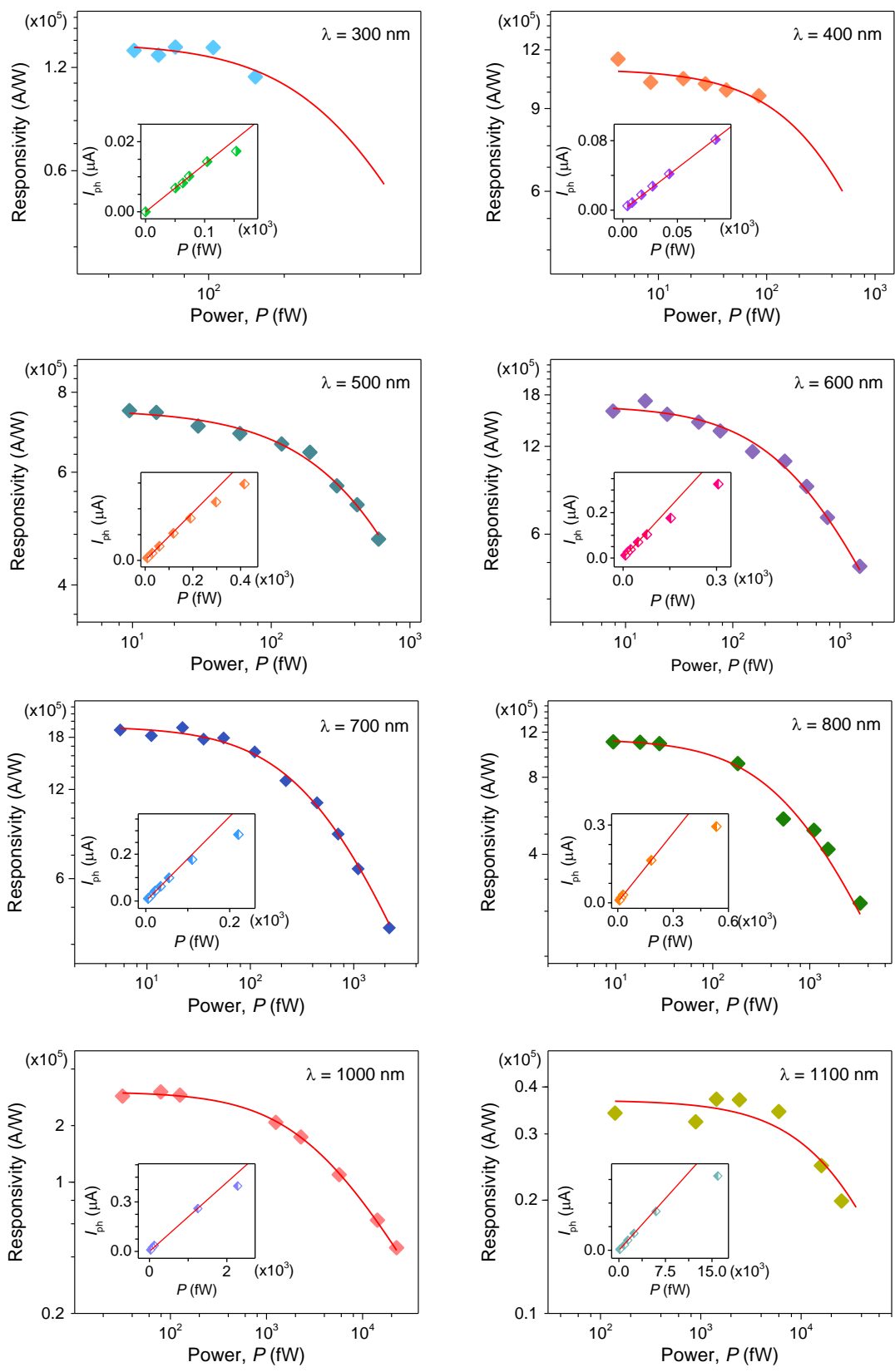


Figure S8. Photo-responsivity as a function of illumination power at different wavelengths.

7. Compare photo-responsivity signal from the substrate of the devices

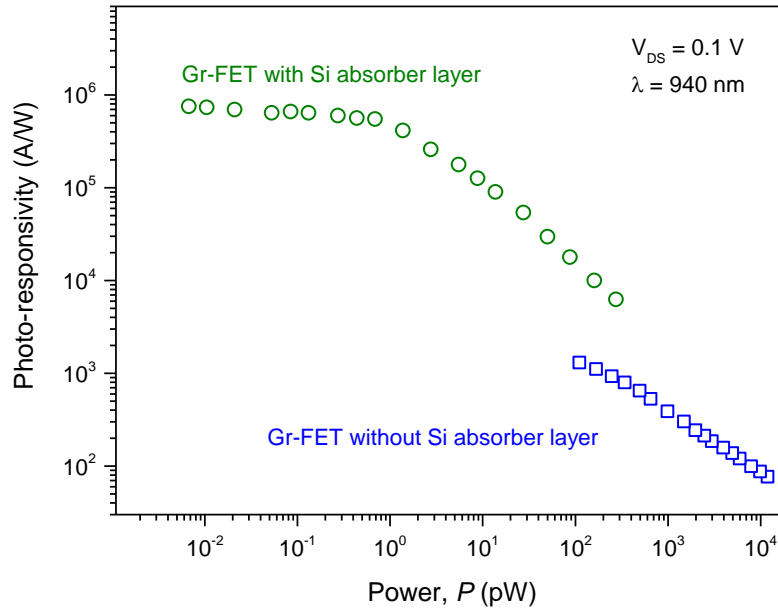


Figure S9. A comparison of the photo-responsivity of graphene Gr-FET devices with and without the silicon absorber layer, showing a weak contribution of the silicon substrate compared with the absorber layer.

8. Noise characterization

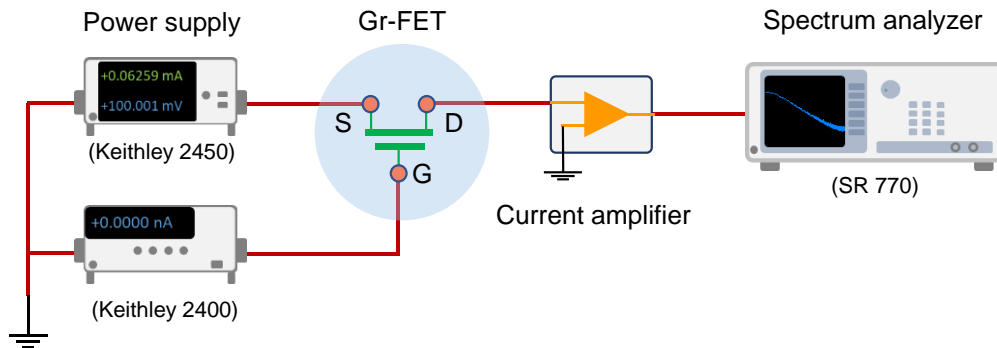


Figure S10. A schematic for $1/f$ noise measurements.

To measure the $1/f$ noise behavior, a Keithley 2450 source-meter unit was used to vary the back-gate voltage, V_{BG} , while another Keithley 2450 source-meter unit was employed to set a drain-source voltage, V_{DS} , at 100 mV. A FEMTO DLPCA-200 low-noise current amplifier was used to amplify the drain current.

A 100 kHz FFT spectrum analyzer (Stanford Research 770 – SR770) was utilized to characterize the noise behavior of the hybrid Si/Gr photodetector without illumination.

The noise equivalent power (NEP) and the specific detectivity (D^*) are important parameters of a photodetector, which can be calculated by investigating the power spectral density of $1/f$, shot, and thermal noise of the Si-Gr photodetectors.

The power spectral density (S_1) of the $1/f$ noise (or the flicker noise) in the dark can be expressed as.¹²

$$S_1(1/f) = \frac{AI_{\text{dark}}^2}{f^\beta}, \quad (\text{S3})$$

where A is the noise amplitude (dimensional less), f is frequency, β is close to 1, and I_{dark} is the dark current of the device. The spectra are dominated by $1/f$ noise up to 1 kHz. The power spectral density of the $1/f$ noise is $8.8 \times 10^{-15} \text{ A}^2/\text{Hz}$.

The power spectral density of shot noise is given by:

$$S_1(\text{shot}) = 2qI_{\text{dark}}, \quad (\text{S4})$$

where q is the elemental charge and I_{dark} is the dark current. The dark current of the photodetectors under $V_{\text{BG}} = 100 \text{ mV}$ is $\sim 39 \mu\text{A}$. The calculated power spectral density of shot noise is $\sim 1.25 \times 10^{-23} \text{ A}^2/\text{Hz}$.

The power spectral density of thermal noise is estimated by Nyquist's equation:

$$S_1(\text{thermal}) = 4k_B T/R \quad (\text{S5})$$

where k_B is the Boltzmann's constant, T is temperature, and R is the differential resistance of the device in the dark. The thermal noise at room temperature is estimated $\sim 6.6 \times 10^{-25} \text{ A}^2/\text{Hz}$.

References

- (1) Wang, Y.; Ho, V. X.; Henschel, Z. N.; Cooney, M. P.; Vinh, N. Q. Effect of High-K Dielectric Layer on $1/f$ Noise Behavior in Graphene Field-Effect Transistors. *ACS Appl. Nano Mater.* **2021**, *4*, 3647-3653.
- (2) Wang, Y.; Ho, V. X.; Henschel, Z. N.; Pradhan, P.; Howe, L.; Cooney, M. P.; Vinh, N. Q. Graphene Photodetector Based on Interfacial Photogating Effect with High Sensitivity. *Proc. SPIE* **2020**, *11503*, 1150306.
- (3) Wang, Y.; Ho, V. X.; Pradhan, P.; Cooney, M. P.; Vinh, N. Q. Graphene-Germanium Quantum Dot Photodetector with High Sensitivity. *Proc. SPIE* **2019**, *11088*, 1108809.
- (4) Ho, V. X.; Wang, Y.; Cooney, M. P.; Vinh, N. Q. Graphene-based photodetector at room temperature. *Proc. SPIE* **2018**, *10729*, 1072907.
- (5) Ho, V. X.; Wang, Y. F.; Cooney, M. P.; Vinh, N. Q. Graphene-Ta₂O₅ heterostructure enabled high performance, deep-ultraviolet to mid-infrared photodetection. *Nanoscale* **2021**, *13*, 10526-10535.

- (6) Malard, L. M.; Pimenta, M. A.; Dresselhaus, G.; Dresselhaus, M. S. Raman spectroscopy in graphene. *Phys. Rep.* **2009**, *473*, 51-87.
- (7) Her, M.; Beams, R.; Novotny, L. Graphene transfer with reduced residue. *Phys. Lett. A* **2013**, *377*, 1455-1458.
- (8) Kim, S.; Nah, J.; Jo, I.; Shahrjerdi, D.; Colombo, L.; Yao, Z.; Tutuc, E.; Banerjee, S. K. Realization of a high mobility dual-gated graphene field-effect transistor with Al₂O₃ dielectric. *Appl. Phys. Lett.* **2009**, *94*, 062107.
- (9) Chen, K.; Wan, X.; Liu, D. Q.; Kang, Z. W.; Xie, W. G.; Chen, J.; Miao, Q.; Xu, J. B. Quantitative determination of scattering mechanism in large-area graphene on conventional and SAM-functionalized substrates at room temperature. *Nanoscale* **2013**, *5*, 5784-5793.
- (10) Wang, N.; Ma, Z. H.; Ding, C.; Jia, H. Z.; Sui, G. R.; Gao, X. M. Characteristics of Dual-Gate Graphene Thermoelectric Devices Based on Voltage Regulation. *Energy technol.* **2020**, *8*, 1901466.
- (11) Baklanov, M.; Green, M.; Maex, K., *Dielectric Films for Advanced Microelectronics*. John Wiley & Sons, Ltd: 2007.
- (12) Kayyalha, M.; Chen, Y. P. Observation of reduced 1/f noise in graphene field effect transistors on boron nitride substrates. *Appl. Phys. Lett.* **2015**, *107*, 113101.